Nonlinear signatures in active microbead rheology of entangled polymer solutions

J. A. Cribb[a)]

Department of Physics, University of North Carolina at Chapel Hill, Chapel Hill, North Carolina 27599

P. A. Vasquez[a),b)]

Department of Mathematics, University of North Carolina at Chapel Hill, Chapel Hill, North Carolina 27599

P. Moore

Dental School, Boston University, Boston, Massachusetts 02215

S. Norris

Department of Cell and Development Biology, University of Michigan, Ann Arbor, Michigan 48109

S. Shah

Medical Scientist Training Program, University of California Los Angeles, Los Angeles, California 90024

M. G. Forest

Department of Mathematics, University of North Carolina at Chapel Hill, Chapel Hill, North Carolina 27599

R. Superfine

Department of Physics, University of North Carolina at Chapel Hill, Chapel Hill, North Carolina 27599

(Received 3 February 2013; final revision received 28 May 2013; published 26 June 2013)

Synopsis

We present experimental data and numerical modeling of a nonlinear phenomenon in active magnetic microbead rheology that appears to be common to entangled polymer solutions (EPS).

[a)]These authors share first author status.
[b)]Author to whom correspondence should be addressed; electronic mail: vasquezpaula02@gmail.com

Dynamic experiments in a modest range of magnetic forces show (1) a short-lived high viscosity plateau, followed by (2) a bead acceleration phase with a sharp drop in apparent viscosity, and (3) a terminal steady state that we show resides on the shear-thinning slope of the steady-state flow curve from cone and plate data. This latter feature implies a new protocol to access the nonlinear steady-state flow curve for biological EPS available only in microliter-scale volumes. We use the moment-closure form of the Rolie–Poly kinetic model for EPS hydrodynamics, together with a decoupling approximation that obviates the need for a full three-dimensional (3D) flow solver, to qualitatively reproduce this dynamic experimental sequence. We thereby explain the phenomenon in terms of entangled polymer physics, and show how the nonlinear event (acceleration and termination on the shear-thinning response curve) is tunable by the interplay between molecular-scale mechanisms (relaxation via reptation and chain retraction) and magnetic force controls. The experimental conditions mimic movement of cilia tips, bacteria, and sperm in mucus barriers, implying a physiological relevance of the phenomenon and compelling further quantitative kinetic-flow 3D numerical modeling. © *2013 The Society of Rheology*. [http://dx.doi.org/10.1122/1.4811477]

I. INTRODUCTION

Microrheology is a technique used to determine the response functions of soft materials that are volume limited or heterogeneous at microscopic length scales. In active microrheology (AM), external forces induce the motion of probe particles, often through the use of optical traps or magnetic fields. Tracking the probe motion allows one to infer linear and, more rarely, nonlinear properties of the medium [Squires (2008); Sriram *et al.* (2009); Squires and Mason (2010)]. Early AM methods by Ziemann *et al.* (1994) applied magnetic forces to beads attached directly to cells and interpreted the results with linear viscoelastic modeling. Subsequent modeling by Uhde *et al.* (2005) described the transient response of pulsed magnetic beads in entangled actin networks as an osmotic pressure effect that arises from the packing of actin filaments in front of the bead, the creation of an entropic restoring force, and subsequent diffusion of the actin bundles to relieve concentration gradients. Recent experiments and modeling by Meyer *et al.* (2006) and Rich *et al.* (2011) interpret nonlinear behavior for probes in colloidal suspensions as shear thinning. Wilking and Mason (2008) used rotating, micron-scale discs in collagen solutions and interpreted nonlinearity as a yield stress. Finally, our own previous work used AM to show steady-state shear thinning for magnetic spheres and nanorods embedded in entangled λ-DNA solutions [Cribb *et al.* (2010)].

Here, we focus instead on the transient dynamics and the asymptotic quasisteady response of magnetically driven microspheres in entangled polymer solutions (EPS) subjected to a controlled, constant force. The range of transient and quasisteady behavior we report, if fully understood and accurately modeled, could have profound implications for characterization of the stress responses induced by objects in motion within many biological systems (e.g., cilia, microswimmers such as sperm and bacteria) and of the transient material properties of the materials through which they travel (e.g., mucus). The primary challenge lies in understanding and modeling the unknown nonlinear mechanisms and responses of EPS, which in turn require determining the unsteady Lagrangian flow field generated by the probe particle as well as the coupled heterogeneous stress distribution that influences its motion; we refer the reader to detailed discussions by Squires (2008), Squires and Mason (2010), Squires and Brady (2005), and Fu *et al.* (2008).

Previously, several proposed numerical and asymptotic methods were used to analyze and model experiments for spheres in viscoelastic fluids falling under gravity in a confined cylinder; for extended discussions on the subject we direct the reader to the work of Arigo *et al.* (1995), Rajagopalan *et al.* (1996), Owens and Phillips (2002), and McKinley

(2002). These studies explain that, while these approaches capture experimental observations in a qualitative way, they do not give quantitative accuracy. The shortcomings are caused by the use of macroscopic constitutive models that coarse-grain the dynamics of the polymer molecular constituents. For this reason, it is imperative to develop mathematical methods capable of coupling microscopic changes in the polymer network with the macroscopic response observed experimentally. To our knowledge, there are no reports of quantitative agreement between computational methods and experimental data for this benchmark problem. It is safe to say that further progress is needed for various classes of complex fluids, and for EPS in particular, to achieve quantitative agreement with experiments.

Most rheological inferences from microrheology experiments rely on the generalized Stokes–Einstein relation (GSER) which gives the diffusivity, D, of a particle with radius a in a medium of viscosity η, $D = k_B T/(6\pi a\eta)$ [Squires and Mason (2010)]. Once experimental conditions violate the assumptions that allow the GSER formulation, the expected agreement between microscopic and macroscopic measurements is lost. Squires and Mason (2010) surveyed conditions under which the Stokes–Einstein relation might fail. For instance, the Einstein component breaks down when actuated probes drive the surrounding polymer system out of equilibrium. Conversely, violations of the Stokes component of the GSER include the presence of particle–material interactions as well as spatial heterogeneities at length scales explored by the particle, i.e., when the particle size becomes comparable to the characteristic length scales of the polymer network. In such instances, interpreting these experimental measurements in a rheologically meaningful way becomes murky.

Here, we report a fundamental signature of nonlinearity found in our experimental data: Beads initially translate uniformly under a constant magnetic force (the expected, canonical, linear Stokes response), then experience a sudden acceleration, followed by convergence to an asymptotic uniform velocity that does not scale linearly with magnetic force. We explain this signature using a mathematical model that includes principles of entangled polymers driven out of equilibrium. We model the evolution of the medium compliance as a function of the applied force and parameters that represent molecular-scale entangled polymer physics. We use the model to qualitatively mimic experimental conditions and timescales, and thereby illustrate modeling capability to tune dynamics of both linear and nonlinear responses.

The constant magnetic force microbead experiments presented here reveal nonlinear phenomena, striking bead acceleration transients and non-Stokesian asymptotic velocities, at modest forces (1–30 pN). We define non-Stokesian asymptotic velocities as those that do not scale linearly with force. The sharp transients in bead velocity, combined with a nonlinear scaling of the asymptotic velocity with magnetic force, imply that the moving bead drives the material out of equilibrium. To fully understand how the instability affects particle mobility, one must explicitly compute the perturbed microstructure surrounding the particle. One strategy to gain quantitative accuracy would require a direct numerical simulation of the controlled magnetic force, a kinetic constitutive model for EPS, as well as the full three-dimensional (3D) momentum balance for the flow field. Instead, we propose a reduced-order model of the fully coupled system that captures the EPS mechanisms by decoupling the flow away from the bead from the extra stresses arising in the polymer network. Our model is computationally feasible and amenable to a wide parameter study, and thereby has the potential to explain the experimental transient phenomena in qualitative terms.

The reduced-order model we developed here provides simulations that can explain the molecular-scale mechanism behind the nonlinear phenomena in both the transients and

the asymptotic quasisteady behavior. In this regard, our experimental-modeling protocol complements the study of individualistic λ-DNA molecular dynamics by Teixeira *et al.* (2007) through the interrogation of nonequilibrium entangled polymer hydrodynamics.

For our experiments, we choose λ-DNA, guar, and hyaluronic acid (HA) solutions because of their relevance in many driven-flow paradigms found in physiology. A significant amount of DNA is present in pathological mucus (sputum), a material the lung must eliminate using cilia propulsion or air drag from breathing and cough to safeguard against infection [Rubin (2006)]. Guar, often used as a thickening agent in foods, has had some success as a mucus simulant when used in mucociliary transport experiments [King and Macklem (1977)]. HA, found throughout the body, is especially instrumental in dissipating stresses in load-bearing joints. The physiological conditions involving these biopolymer solutions comprise a wide range of forcing at transient shear rates, suggesting that nonequilibrium fluid dynamical phenomena play essential roles in human physiology. The thresholds of nonlinear response and possible signatures of nonlinearity in human physiology drive the motivation for this study.

II. MATERIALS AND METHODS

A. Sample preparation

We prepared our λ-DNA solution (Invitrogen, Carlsbad, CA, 25250-028), at a concentration of 1.4 mg/ml by concentrating stock λ-DNA with centrifuge filters (Amicon Ultra UFC510024) that had a molecular weight cutoff of 100 kD. A λ-DNA solution at this concentration should be in the entanglement regime, i.e., above the overlap concentration, $c^* = 0.07$ mg/ml. This solution contains an average of 20 entanglements per chain, a reptation time of 3.2 s, and a plateau modulus of 0.9 Pa. The guar reagent, derived from the seeds of *Cyamopsis tetragonoloba*, presented large aggregates (30 μm) of structural matrix and cellular debris. To avoid spatial heterogeneities it became necessary to eliminate these large aggregates using centrifugation (15 000 g for 10 min) at little to no cost of its macroscale rheology, confirmed via cone and plate (CAP) measurements. The guar solution, prepared at a concentration of 15 mg/ml, is also in the entanglement regime ($c^* = 0.3$ mg/ml) with an average of 50 entanglements per chain, a reptation time of 0.75 s, and a plateau modulus of 49 Pa. Finally, the HA solution (Sigma-Aldrich 53747), prepared at 10 mg/ml, is in the semidilute regime (since $c^* = 10$ mg/ml), has a reptation time of 0.2 s and a plateau modulus of 46 Pa. We obtained the molecular weight for each solution from the manufacturer or measured using light scattering techniques. We calculated the contour length and number of entanglements per chain using persistence lengths obtained from published work by Lu *et al.* (2002), Morris *et al.* (2008), and Buhler and Boué (2004). Finally, we found reptation time and entanglement modulus for each solution through fitting CAP data to the Rolie–Poly model as described in Sec. V.

B. Microrheology experiments

Our magnetic-tweezer system, described previously by Fisher *et al.* (2006), uses a small angle thin-foil wedge of magnetically permeable metal, referred to here as a "pole-tip," mounted to a glass coverslip, which is, in turn, mounted onto miniature copper-wire coils capable of driving up to 2.5 A of DC current with an operating bandwidth of 20 kHz (Fig. 1). This pole-tip and coverslip act as the upper boundary of the sample chamber while a plain coverslip serves as its lower boundary. We load a small volume (1–3 μl) of specimen inside the sample chamber and place the entire assembly into a Nikon TE-2000

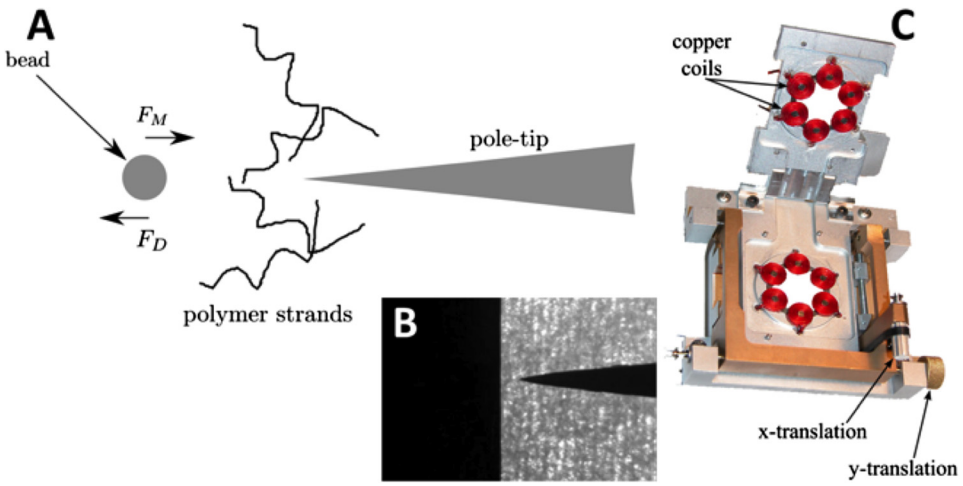

FIG. 1. (A) Schematic of experiment: The bead experiences a magnetic force, F_M, from the pole-tip that is countered by the drag F_D of the surrounding solution. (B) Photo of pole-tip, tip radius is approximately 15 μm. (C) Magnetics system where pole-tip is mounted to one of the several available copper-wound coils. Each coil surrounds a permalloy core that comes into magnetic contact with the nearby pole-tip. When current flows through the coil magnetic flux is channeled into the pole-tip, generating an intense magnetic field in the proximity of beads embedded inside the polymer solution.

inverted microscope outfitted with a 60×1.2 numerical aperture (NA) water-immersion objective.

Embedded inside each specimen solution are 1 μm diameter magnetic beads (Dynal MyOne) whose surfaces are functionalized with polyethylene glycol to discourage any intrinsic attachment to the surrounding polymer system. Flowing current through the magnetic coil channels magnetic flux through the pole-tip, generating a magnetic field that attracts the magnetic beads distributed throughout the specimen volume. Applying a step current generates a step force, F_M, over small bead excursions x(t) (<5 μm) that range from 1 pN at a distance of 100 μm from the pole-tip to 1000 pN at the pole-tip surface. Because the pole-tip itself imposes a no-slip boundary condition to the sampling space, we limited ourselves to locations that were 10 or more bead diameters away from the pole-tip, effectively reducing our applicable force to approximately 150 pN. To measure creep response, we applied step currents that could range between 0.12 and 2.5 A for durations that lasted from 0.2 to 15 s. A Jai Pulnix PTM-6710 camera collected images at 120 frames per second, equivalent to an 8.6 ms temporal resolution. Once collected, bead trajectories were tracked offline using our custom spot tracking software (www.cismm.org) [Fisher *et al.* (2006)].

C. CAP rheometry

To compare our microrheology measurements with classical macroscopic measurements, we employed a stress-controlled rheometer (AR-G2, TA Instruments, DE) and its 40 mm diameter/1° CAP geometry. For dynamic measurements, the instrument applied a constant shear rate (in feedback) and recorded the evolution of the shear stress, τ_{xy}, as a function of time. We used the long time scale, steady-state values to create a flow curve of viscosity, η, versus shear rate, $\dot{\gamma}$, where $\eta = \tau_{xy}/\dot{\gamma}$. The Stokes solution for the drag force, F_D, on a bead of radius a that is moving at constant speed U, provides the maximum shear rate at the bead surface, $\dot{\gamma} = 3U/\sqrt{2a}$.

III. MATHEMATICAL MODELING

We model the transient motion of a spherical probe of radius a and mass m accelerating in a polymeric fluid under the influence of a constant applied magnetic force, F_M. If the applied magnetic force and the drag force on the bead are equal, Stokes drag law gives the apparent viscosity, η_{app}, as

$$\eta_{app} = \frac{F_D}{6\pi a U}, \quad \text{with } F_M = F_D. \tag{1}$$

When $F_M \neq F_D$, a balance between these two forces gives the instantaneous change in the velocity of the probe, $U(t)$

$$m\frac{dU(t)}{dt} = F_M - F_D(t). \tag{2}$$

We obtain the drag force acting on the probe by integrating the normal traction over its surface, S

$$F_D = \oint\left[\left(-p\boldsymbol{I} + 2\eta_s\{(\nabla \boldsymbol{v}) + (\nabla \boldsymbol{v})^T\}\right)\cdot\hat{\boldsymbol{n}} + (\boldsymbol{\sigma} - \boldsymbol{I})\cdot\hat{\boldsymbol{n}}\right] dS, \tag{3}$$

where $\hat{\boldsymbol{n}}$ is the inward-pointing unit normal vector, η_s is the viscosity of the solvent, $\boldsymbol{v}$ is the velocity field induced by the probe's displacement, p is the isotropic pressure, $\boldsymbol{I}$ is the identity tensor, and $\boldsymbol{\sigma}$ is the extra stress tensor arising from conformational changes of the entangled polymer molecules immersed in the solvent [Bird *et al.* (1987)].

Closing the system of Eqs. (2) and (3) requires a constitutive equation for $\boldsymbol{\sigma}$; here, we use the Rolie–Poly model for EPS formulated by Likhtman and Graham (2003). In this model, the evolution of the extra stress is given by

$$\frac{d\boldsymbol{\sigma}}{dt} = (\nabla \boldsymbol{v})^T\cdot\boldsymbol{\sigma} + \boldsymbol{\sigma}\cdot(\nabla \boldsymbol{v}) - \frac{\boldsymbol{\sigma}-\boldsymbol{I}}{\tau_d} - \frac{2}{\tau_R}\left(1 - \sqrt{\frac{3}{tr(\boldsymbol{\sigma})}}\right)\left[\boldsymbol{\sigma} + \beta\sqrt{\frac{3}{tr(\boldsymbol{\sigma})}}(\boldsymbol{\sigma}-\boldsymbol{I})\right]. \tag{4}$$

Within this constitutive equation, two characteristic timescales govern the dynamics of the polymer network: The relaxation by chain orientation, described by the *reptation time* $\tau_d = 3Z^3\tau_e$, and the relaxation by chain stretch given by $\tau_R = Z^2\tau_e$ [Likhtman and Graham (2003)]. Here, τ_e is the *Rouse relaxation time* of an entanglement segment and Z is the *number of entanglement segments* in a chain. In addition, the parameter $0 \leq \beta \leq 1$ captures the effects of *convective constraint release*. In this study, we fix $\beta = 1$, following the work of Teixeira *et al.* (2007) and Likhtman and Graham (2003). This implies that, in this work, the only two fitting parameters are Z and τ_e.

To solve the resulting system of equations, we impose a flow decoupling approximation that allows us to determine a closed-form expression at each time step for the velocity field external to the bead. Our modeling assumptions allow us to bypass a full solution of all hydrodynamics and stress fields in space and time. Specifically, we assume that the bead translational velocity at each time step, $U(t)$, generates an instantaneous quasisteady Stokes velocity field. The velocity field is thereby explicit; in spherical coordinates and assuming axisymmetric flow ($v_\phi = 0$), this field is given by [Pozrikidis (1997)]

$$[v_r, v_\theta] = \frac{U(t)}{2}\frac{a}{r}\left[\cos\theta\left(3 - \left(\frac{a}{r}\right)^2\right), -\frac{\sin\theta}{2}\left(3 + \left(\frac{a}{r}\right)^2\right)\right]. \tag{5}$$

Here v_r and v_θ are, respectively, the velocity components in the r and θ directions. Equation (5) then yields the velocity gradient tensor, $\nabla \boldsymbol{v}$, at the surface of the bead, $a = r$.

Once the velocity field around the bead is determined from Eq. (5), Eqs. (2)–(4) constitute a nonlinear integro-differential system of equations that provide a closed dynamical representation of bead motion and surface stresses. The initial conditions at $t = 0$ assume that the polymer molecules are at equilibrium so that $\boldsymbol{\sigma} = \boldsymbol{I}$, and from the Stokes relation (1) we impose an initial value for the velocity of the probe that assumes an initial Stokes response speed

$$U(0) = \frac{F_M}{6\pi a \eta_s}. \tag{6}$$

To impose the boundary conditions, we update the local conformational distribution of the polymer molecules at the bead surface and calculate the extra stress using the Rolie–Poly constitutive equation.

In this study, we show this approximate model is sufficient to capture the experimentally observed behavior. Because of its relative computational simplicity, we can explore a wide range of model parameters to mimic experimental controls as well as EPS molecular properties, and analyze both transient and quasisteady behavior across the full parameter space. We also note that the standard linear viscoelastic protocol measures the steady-state velocity, U_∞, and assumes that the only forces on the probe are due to viscous drag and magnetic forces, using Eq. (1) to get the viscosity. Our extension of this protocol models a nonuniform bead motion and the forces on the bead that arise from nonequilibrium microstructure-induced stresses. Since the force balance at the bead surface governs the bead velocity $U(t)$, the viscosity of the fluid evolves in time through shear thinning and thickening states when there are non-negligible microstructure-induced stresses. Our goal with the approximate model is to identify the underlying molecular basis for the conformational dynamics of the entangled polymer molecules that result in bead takeoff events and that emerge in the convergence to non-Stokesian quasisteady velocities.

To find the state of the dynamical system (2)–(5) at $t + \Delta t$, we follow the protocol defined explicitly here and illustrated as a flowchart in Fig. 2. First, we use the bead velocity at time t, $U(t)$, to evaluate the velocity gradient tensor, $\boldsymbol{\kappa} = (\nabla \boldsymbol{v})^T$ at the bead surface through Eq. (5). We then update the extra stress by integrating Eq. (4) using a semi-implicit finite difference scheme. We then use this extra stress $\boldsymbol{\sigma}$, to compute the new drag force on the sphere via Eq. (3). Finally, we use this new drag force to update the bead velocity using Eq. (2). In this way, Eqs. (2)–(5) constitute a closed seven-dimensional nonlinear dynamical system for $U(t)$ and $\boldsymbol{\sigma}(t, a, \theta)$, given a magnetic force, F_M, and a bead diameter, a.

Finally, for completeness, we note that, when the nonlinear stress terms in the Rolie–Poly equation (4) are sufficiently small, the model reduces to the upper convected Maxwell (UCM) model

$$\frac{d\boldsymbol{\sigma}}{dt} = (\nabla \boldsymbol{v})^T \cdot \boldsymbol{\sigma} + \boldsymbol{\sigma} \cdot (\nabla \boldsymbol{v}) - \frac{\boldsymbol{\sigma} - \boldsymbol{I}}{\tau_d}. \tag{7}$$

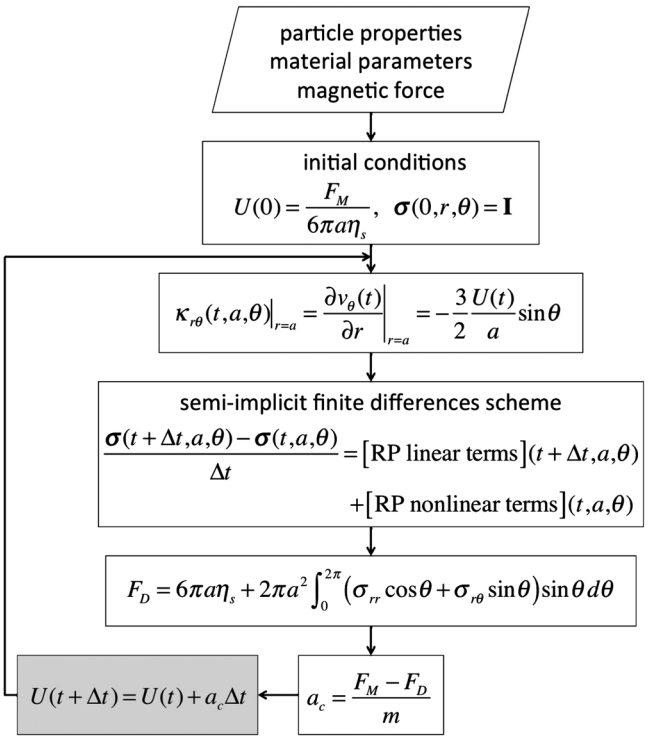

FIG. 2. The model and flowchart used to solve the system of Eqs. (2)–(5).

Since $(\nabla \boldsymbol{v})$ is given at the bead surface, the UCM model is exactly solvable, which we shall exploit to illustrate the necessary role of the Rolie–Poly nonequilibrium model mechanisms in capturing the nonlinear bead dynamic phenomena.

To find the steady-state solution to the UCM model, we posit the functional form of the stress as in the linear viscoelastic case and introduce the following transformations:

$$\sigma_{rr} = g(t)\sin^2\theta + 1, \tag{8a}$$

$$\sigma_{r\theta} = f(t)\sin\theta. \tag{8b}$$

Then, the drag force is explicitly given by

$$F_D = 6\pi a\eta_s + \frac{8}{3}\pi a^2 f(t). \tag{9}$$

The resulting system of differential equations is

$$\frac{dg(t)}{dt} = \frac{3}{a}U(t)f(t) - \frac{1}{\tau_d}\ g(t), \tag{10a}$$

$$\frac{df(t)}{dt} = \frac{3}{2a}\frac{\eta_p}{\tau_d}U(t) - \frac{1}{\tau_d}\ f(t), \tag{10b}$$

$$\frac{dU(t)}{dt} = \frac{1}{m}\left[F_M - 6\pi a\eta_s U(t) - \frac{8}{3}\pi a^2 f(t)\right]. \tag{10c}$$

Here, η_p is the zero-shear rate viscosity of the polymeric fluid. The steady-state solution of Eqs. (10) is likewise explicit

$$U_\infty = \frac{F_M}{6\pi a(\eta_s + 2/3\ \eta_p)}, \tag{11a}$$

$$f_\infty = \frac{3}{2a}\eta_p U_\infty, \tag{11b}$$

$$g_\infty = \left(\frac{3}{\sqrt{2}a}\right)^2 \tau_d \eta_p U_\infty^2. \tag{11c}$$

Analysis of the dynamical system (10) confirms that the steady state (11a)–(11c) is a unique stable attractor. Thus, for polymeric solutions described by the UCM model, Eq. (11a) gives the asymptotic bead velocity uniquely. Clearly, the steady-state velocity for a linear viscoelastic or UCM model fluid is linear in the magnetic force, with the same Stokesian scaling as a viscous fluid and an "effective" viscosity $\eta_{eff} = \eta_s + 2/3\ \eta_p$.

We have thereby recovered the standard linear viscoelastic rheological inference for magnetic microbeads under constant forcing. That is, given F_M, a, and the measured U_∞ (confirmed to scale linearly with F_M) one can infer the effective viscosity, η_{eff}.

IV. EXPERIMENTAL RESULTS AND OBSERVATIONS

Our first bulk measurements show the transient/dynamic response of our test materials to a step strain rate measurement imposed by the CAP rheometer. All three solutions show a linear viscoelastic response at a shear rate $\dot{\gamma} = 0.1\ \text{s}^{-1}$, where the apparent viscosity is a monotonic function of time (Fig. 3). Higher shear rates reveal nonlinear responses for guar and DNA solutions, detected by a viscosity overshoot. The guar solution shows a viscosity overshoot at a shear rate of $\dot{\gamma} = 10\ \text{s}^{-1}$, and for the DNA data, extracted from Teixeira *et al.* (2007), this occurs at $\dot{\gamma} = 30\ \text{s}^{-1}$. We note that both of these solutions are at concentrations much higher than their overlap concentration, c^*. Conversely for the HA solution, which has a lower concentration relative to c^*, overshoots appear at much higher shear rates than the ones shown in the figure.

We also used bulk CAP methods to measure the steady-state rheology of our solutions. Shown in Fig. 4 as solid lines is the steady-state apparent viscosity of each solution plotted against the Weissenberg number, $We = \dot{\gamma}\ \tau_d$, where τ_d is the longest relaxation time (Table I). These results show that all solutions investigated in this study exhibit shear thinning for $We \sim 1$, which, in turn, implies that larger shear rates are necessary to observe shear thinning in the HA data, consistent with Fig. 3. Namely, we expect DNA to shear thin, and hence show overshoots in plots of viscosity versus time, for shear rates $\dot{\gamma} \sim 1/3.2 = 0.31\,\text{s}^{-1}$; for guar this is $\dot{\gamma} \sim 1/0.75 = 1.33\,\text{s}^{-1}$, and for HA $\dot{\gamma} \sim 1/0.2 = 5\,\text{s}^{-1}$.

In the microbead experiments, instead of direct stress and strain measurements that the CAP provides, our instrument generates displacement curves by tracking bead trajectories over time while under a constant applied force, F_M. Figure 5 shows trajectories for

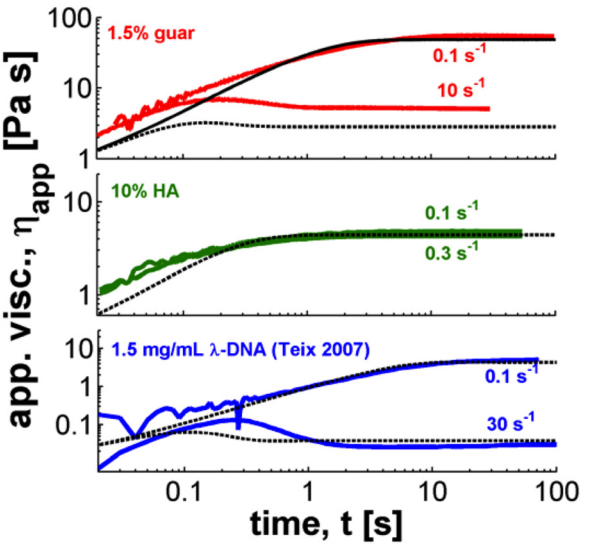

FIG. 3. Apparent viscosity η_{app} for steady, shear-rate-mode CAP data (colored curves) on three polymeric solutions, with fits to the Rolie–Poly model (black curves). The shear rates shown here were chosen to match those accessible by the magnetic system.

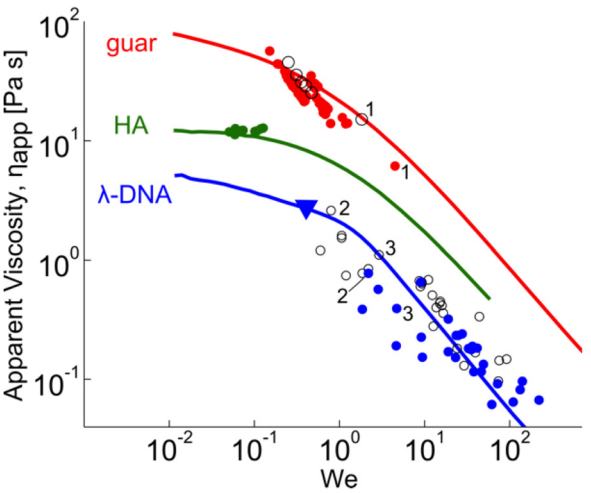

FIG. 4. Measured η_{app} of λ-DNA, guar, and HA solutions versus shear rate in CAP (solid lines) and in the magnetic-tweezer system where open symbols correspond to measurements at U_0 and closed symbols at U_∞, each obtained from the appropriate regimes shown in detail in Figs. 5 and 6. Numerical labels indicate representative U_0 and U_∞ pairs.

TABLE I. Molecular weight M_w, contour length L_c, concentration nc^*, number of entanglements per chain Z, reptation time τ_d, and entanglement modulus G_e of each polymeric system.

	M_w (MDa)	L_c (μm)	nc^*	Z	τ_d (s)	G_e (Pa)
Guar	50	54	46	50	0.75	49
HA	1.6	0.5	1	1	0.2	46
λ-DNA	32	14.7	18	20	3.2	0.86

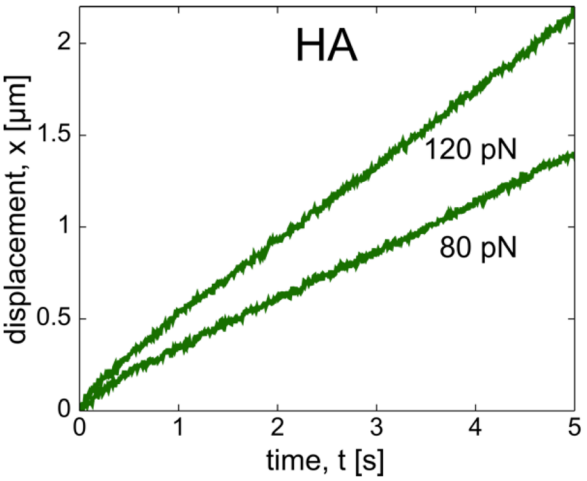

FIG. 5. Bead displacements in HA showing the scaling of steady-state velocity consistent with linear rheological behavior and Stokes drag.

beads embedded in the HA solution, revealing a typical Stokes response for any force accessible with our experimental setup.

When we apply the same type of measurement for beads embedded within DNA we also find the typical Stokes response, but only for forces below a threshold, i.e., when $F_M \leq F_T$, where F_T is approximately 2 pN, as shown in Fig. 6. Below F_T, the bead dynamics quickly reach a steady-state velocity (U_∞). Above F_T, a remarkable dynamic transition sequence occurs: First an initial, apparently steady, velocity U_0, followed by a bead acceleration phase and subsequent saturation to a terminal velocity U_∞ that scales nonlinearly with the applied magnetic force F_M (Fig. 6). The ratio U_0:U_∞ in our experimental datasets ranges from 1:2 to 1:10. Guar data, not shown here, exhibit the same acceleration events as DNA. For both DNA and guar, we distinguish linear from nonlinear asymptotic response when U_∞ fails to scale linearly with F_M.

Importantly, the timescales of the initial Stokes response U_0 and the acceleration phase are potentially below experimental resolution, easily leading one to misinterpret the asymptotic steady velocity, U_∞, as a linear Stokes response and thereby report an erroneous Stokes viscosity. Therefore, the detection of the nonlinear threshold force F_T is critical, and it follows by the force sweep protocol and scaling of bead displacement.

We infer the apparent viscosity η_{app} from both U_0 and U_∞ using Stokes drag law [Eq. (1)], and plot these values in Fig. 4 as discrete data points. Remarkably, $\eta_{app}(U_0)$ and $\eta_{app}(U_\infty)$ lie, within experimental error, on the viscosity versus shear rate curve from CAP experiments for all three biopolymer solutions. Further, for trajectories that show a bead acceleration event, the asymptotic data always lie on the shear-thinning part of the curve. It is clear that for HA, the applied forces cannot generate sufficiently large shear rates to shear thin the solution, in accord with CAP measurements; thus all AM data for HA lie on the viscosity plateau at low shear rates as expected for a viscoelastic material in the linear response regime.

V. MODELING: RESULTS AND DISCUSSION

Numerical solutions to the system of Eqs. (2)–(5) show that, at short times, the bead displacement exhibits a linear Stokes response [Fig. 7(A)], i.e., a deceleration from the posited

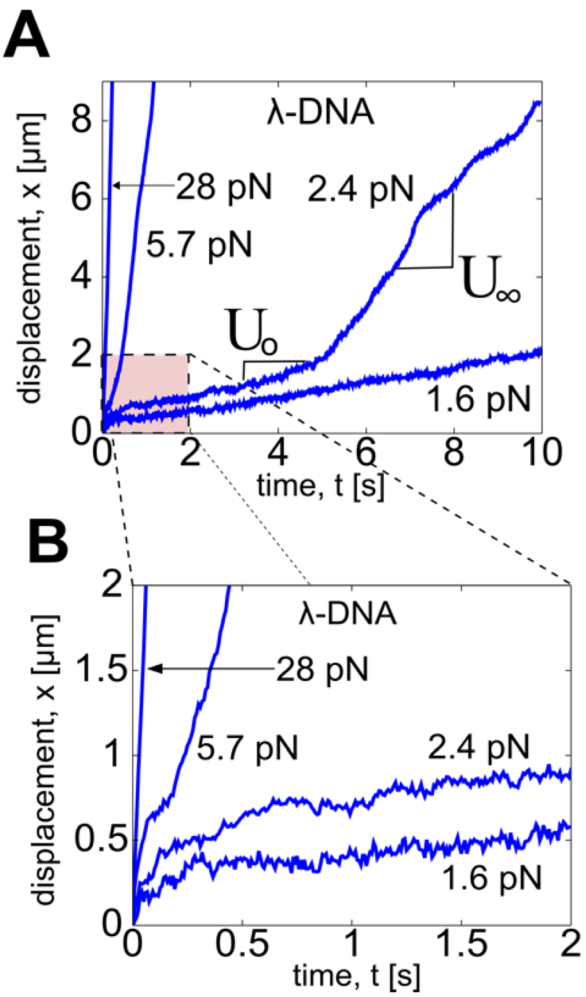

FIG. 6. (A) Bead displacements in λ-DNA for constant applied forces. Note transition from U_0 to U_∞ in the 2.4 pN trajectory. (B) Zoom-in of early responses in (A) showing transition for the 5.7 pN trajectory.

initial velocity $U(0) = F_M/6\pi a\eta_s$. This deviation from the initial velocity comes from the change in the drag force that results from a nonzero viscoelastic stress in Eq. (3). Since, as discussed above, in this linear regime viscoelastic stresses contribute to the effective viscosity giving $\eta_{eff} = \eta_s + 2/3\ \eta_p$. This initial regime is shown in Figs. 7(B) and 7(C) at $t < 10^{-2}$ s. In Fig. 7(B), we show simulated bead displacements versus time for different values of the number of chain entanglements, Z. At small values of Z, bead takeoff is absent. As the number of entanglements increases, the system is driven out of equilibrium, as shown by the onset of bead takeoff events at the same applied force. Beyond the initial Stokes regime, the bead velocity either plateaus to a single value or transitions between two states, depending on the applied force. We first analyze this transition in terms of the applied force by keeping the model parameters, τ_e and Z, constant.

As before, we designate F_T as the threshold value for the applied force that differentiates the two responses described above. For the parameter values used in Fig. 7(C), we found that $F_T \sim 3$ pN. When $F_M < F_T$ the nonlinear corrections to the standard linear viscoelasticity are negligible, and the velocity scales linearly with the magnetic force, or equivalently, the lower set of compliance curves in Fig. 7(C) overlap at all times. In these

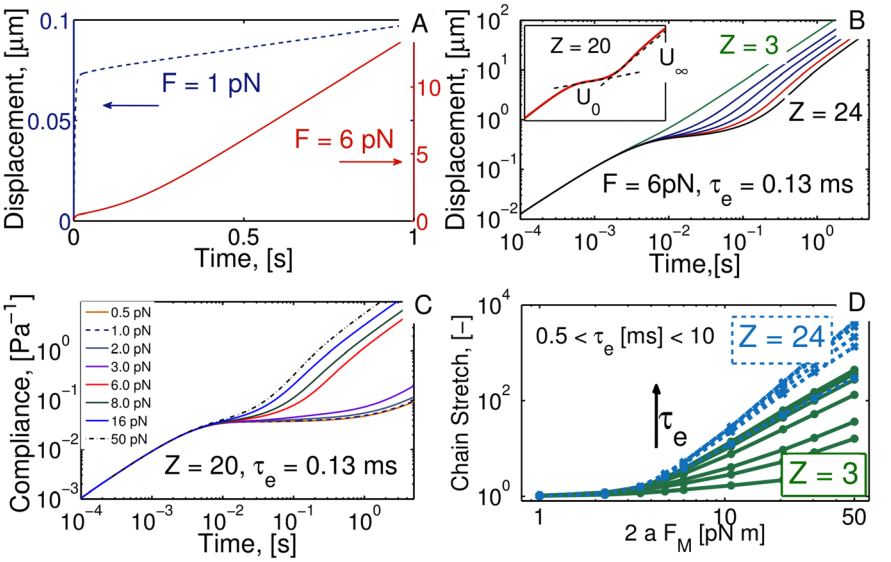

FIG. 7. Rolie–Poly model simulations. (A) Lin-Lin plot of the predicted displacement X for beads driven by low (blue-dashed) and high (red) F_M, producing linear and nonlinear responses, respectively. (B) Log–log plot of displacement versus time as a function of Z. Increasing Z invokes a nonlinear response. (C) Log–log plot of compliance $(6\pi aX/F_M)$ versus force plots show that these curves do not overlap, indicating nonlinear material response. (D) Log–log plot of chain stretch $[tr(\boldsymbol{\sigma})/3]$ versus applied force. Recall that $tr(\boldsymbol{\sigma})/3 = 1$ for chain configurations close to equilibrium.

conditions, there is no bead takeoff event. The mild upturning of the compliance plots is associated with convergence to a Stokes steady-state velocity. In this figure, compliance is found by scaling bead displacement by $6\pi a/F_M$.

As F_M increases past the threshold value, the bead transitions from an apparent Stokes velocity, U_0, through an acceleration phase followed by convergence to a terminal constant velocity, U_∞. This terminal velocity does not scale linearly with F_M, as seen by the shift in the high compliance curves in Fig. 7(C), recapitulating the experimental data discussed previously.

Now, we turn our attention to the dependence of bead displacement history on model parameters. In order to distinguish the critical role played by entanglement dynamics, we take the limit $\tau_R \to \infty$, which reduces the Rolie–Poly model to the UCM model. As determined above analytically, solutions of the UCM model do not exhibit bead acceleration events for any set of parameters. We conclude that the experimental phenomenon of interest here is not due to pure chain orientation dynamics. Instead, we focus our investigations on stretching and retraction dynamics, governed by τ_R, and consider their effects on transient shear thickening and thinning events.

Within the Rolie–Poly model the normalized trace of the conformation tensor, $tr(\boldsymbol{\sigma})/3$, gives the end-to-end stretch of the average polymer chain. Therefore, within our analysis of chain stretching and retraction dynamics, we can use $tr(\boldsymbol{\sigma})/3$ as a metric to detect nonlinear behavior and bead takeoff dynamics. Additionally, the nonlinear terms in Eq. (4) vanish when $tr(\boldsymbol{\sigma})/3 \sim 1$, implying that the chains are near equilibrium. Our numerical investigation of the model parameter space shows that bead takeoff events occur when $tr(\boldsymbol{\sigma})/3$ is $O(10)$ or larger.

As a first step in understanding the role that chain stretching dynamics plays in the bead takeoff phenomena, we explore in Fig. 7(D) the steady-state behavior of $tr(\boldsymbol{\sigma})/3$ as a function of F_M, ZZ, and τ_e. When the number of entanglements is small ($Z = 3$ in the

figure), chain stretching increases significantly with increasing entanglement relaxation time, τ_e. In this semidilute regime, chains cannot relax to their equilibrium configuration within time scales comparable to those of the applied deformation. Here, the relaxation of individual entanglement segments plays a crucial role in the relaxation dynamics of the whole chain. Further increase in Z, with a constant force, results in an increase in chain stretching; however, in this case the dependence on τ_e is weaker. This arises because, for larger Z, the entangled *network* of chains dominates the relaxation dynamics, rather than the entanglement *segments*. This behavior of the chain stretching and the fact that $tr(\boldsymbol{\sigma})/3$ is directly related to bead takeoff events strongly suggest that the magnitude of the deformation and the ability of the network to relax after the deformation play a major role in the bead takeoff dynamics.

So far, we have shown how changes in the steady-state values of chain stretch signal a nonlinear microstructural transition governing the bead acceleration events. Next, we focus on the analysis of the temporal evolution of stress around the bead to reveal the mechanisms and timescales involved in this departure from linear behavior. Figure 8 depicts a surface plot generated by a family of constant-shear-rate solutions of Eq. (4) using parameter values for λ-DNA given in Table I trajectories at long times reproduce $\eta_{app}(U_\infty)$, consistent with experimental data on the steady-state shear-thinning curve in Fig. 4. The dashed yellow curves correspond to the traditional viscometric CAP measurements with a controlled, constant shear rate. Solutions of the system (2)–(5) give $\eta_{app}(t) = \sigma_{r\theta}(t)/\dot{\gamma}(t)$, plotted as solid red curves in Fig. 8 while their respective projections onto the surface are shown as white dashed curves. Here, the unsteady nature of the Lagrangian flow field around the bead is evident as the shear rate and viscosity change in time, transverse to lines of constant shear rate.

In Fig. 9, the simulated bead trajectories (red) are plotted together with lines of constant shear rate (black). From this figure, we note that the viscosity overshoot experienced by the bead is larger in experiments where the force is constant, compared to those where the velocity is constant. Nonetheless, since the beads asymptotically approach a constant U_∞, and thus a constant $\dot{\gamma}_\infty$, the Rolie–Poly simulations of viscosity versus shear rate recover the CAP steady-state shear-thinning curve.

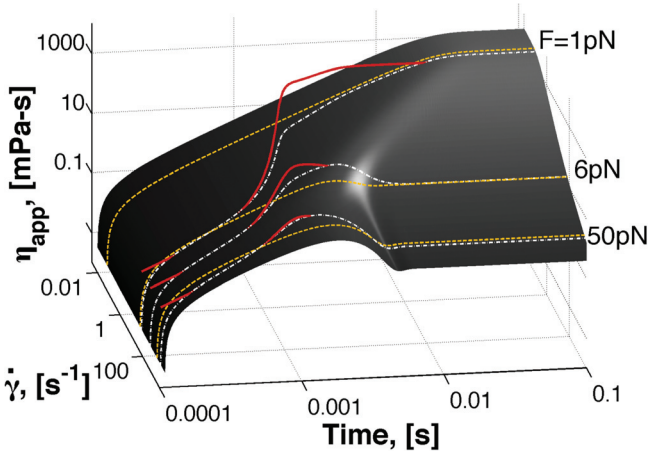

FIG. 8. Surface of apparent viscosity, η_{app}, versus time, obtained from solutions of the Rolie–Poly model with imposed constant shear rate, $\dot{\gamma}(t)$. Three examples of CAP experiments are shown in yellow curves, which correspond to experiments with constant shear rate. Red curves correspond to Rolie–Poly simulations of magnetic bead trajectories with their surface projections shown as white dashed lines. Recall that the initial condition for the bead trajectories (red lines) is $U(0) = F_M/6\pi a\eta_s$, in our simulations $\eta_s = 0.005$ Pa s and $a = 0.5$ μm.

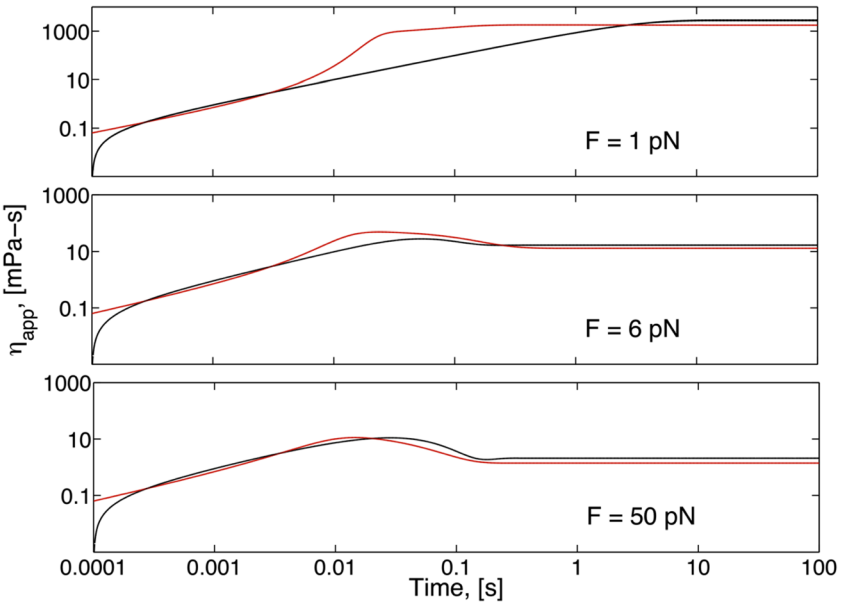

FIG. 9. Simulated bead trajectories (red lines) projected upon planes of constant shear rate (black lines) in the surface shown in Fig. 8. This figure shows that the viscosity overshoot experienced by a bead pulled at a constant force is larger than the overshoot experienced by a bead pulled at a constant velocity.

These observations indicate that a necessary condition for bead takeoff is that the bead trajectory must pass through a region of viscosity overshoots. Because the shear history on a bead can take any "trajectory" for a given set of parameters, this illustrates the tunability of the nonlinear behavior. For bead trajectories with a takeoff event, the duration of U_0 depends on how soon the dynamic viscosity trajectory leaves the overshoot region. The time scale of this transition depends on the strength of the deformation, which is a function of F_M, and on the surface shape, itself dictated by the polymer chain parameters, Z and τ_e. The formalism we have developed here using the Rolie–Poly model qualitatively illustrates the bead takeoff phenomena as the interplay between nonlinear relaxation dynamics of the polymer network and rate of deformation imposed by the pulling bead.

VI. CONCLUSIONS

In summary, we presented and then interpreted experimental trajectories of magnetically driven microbeads in EPS that, with a tunable magnetic force, transition from a linear to a nonlinear response. Our mathematical modeling qualitatively reproduces the full dynamic sequence of linear and nonlinear bead experiments, with a tradeoff in quantitative accuracy based on a flow decoupling approximation that renders the bead dynamics and the evolution of the surrounding microstructure numerically tractable. The Rolie–Poly model for EPS is used to afford a microstructural interpretation of the nonlinear behavior.

Above a critical magnetic force, the traveling bead distorts the surrounding entangled network from its equilibrium conformation and generates extra stresses stored by

nonequilibrium network and chain conformations. These extra stresses, enhanced by the drag force on the bead, drive the bead out of the linear Stokes regime at nonconstant speeds until conformational stresses equilibrate with the applied force, thus dictating the asymptotic bead velocity. The response of the entangled polymer network to the imposed deformation consists of an interplay between the rate of deformation imposed by the bead and the rate of retraction of the entanglement segments toward their equilibrium configuration. As the pulled bead translates through the entangled network, the imposed deformation extends and orients the flexible polymer chains in the network. This conceptual picture forms the basis of the model presented by Uhde *et al.* (2005), demonstrating that the protocol presented here can be applied to other complex fluids, although the choice of constitutive equation depends upon the particulars of the polymeric microstructure.

The Rolie–Poly model, based on tube theory, states that the equilibration time of the chain contour length is much faster than the relaxation time of the chain orientation. When the force pulling the bead is small, the chains conserve their equilibrium contour length under the applied deformation and the entangled network deforms much more slowly than the stretch/retraction relaxation rates of the network. A viscosity that is a monotonic function of time characterizes this behavior in CAP data, while a single asymptotic bead velocity is the signature in the pulled bead experiments. Conversely, when the rate of equilibration by contour length fluctuations is comparable to the deformation rate, the bead experiences significant microstructural changes in the network characterized by viscosity overshoots in CAP data and a transition between two velocities in the microbead experiments. In this case, an initial accumulation of strains impedes the bead motion until network relaxation occurs. Finally, if the applied force is too large, the bead moves through the overshoot very quickly, giving the appearance of linear Stokes behavior when it is in fact a shear-thinned response. Since the time scale of the viscosity overshoots is related to the relaxation of chain stretching, this last scenario occurs when the deformation rates exceed the rate of relaxation by contour length fluctuations.

We emphasize that the *qualitative* behavior with our modeling is not unique to the Rolie–Poly conformation tensor model. Simulations with alternative nonlinear conformation tensor models, the Giesekus model, for example, are also able to capture these nonlinear microbead phenomena. We choose the Rolie–Poly model because its parameters have molecular and network significance for EPS, and we believe that a fully resolved kinetic Rolie–Poly equation, flow field, and bead motion model have the potential to yield more quantitative accuracy. Our results make a compelling case for the investment in such a full 3D kinetic-flow-microbead algorithm. Such a modeling tool would complement high-resolution magnetic bead experiments and provide deeper understanding of the intrinsic dynamics underlying nonlinear mechanisms in EPS.

The physiological relevance of the observed overshoot in the apparent viscosity becomes more clear when we consider the Weissenberg number $We = \dot{\gamma}\tau_d$, where $We > 1$ describes the regime for shear thinning. We highlight three examples where objects move through mucus, characterized to have a reptation time $\tau_d \sim 40$ s [Puchelle *et al.* (1987)]. In the lung, 250 nm diameter cilia tips move with velocities of $\sim$200 μm/s, resulting in a $We = O(10^6)$ (Hill *et al.*, 2010). Bacteria, with diameters of 1 μm, swim through mucus at velocities of $\sim$30 μm/s [Celli *et al.* (2009)], giving $We = O(10^3)$. The acrosome of sperm has a diameter of $\sim$5 μm and a velocity of 30 μm/s, we calculate a $We = O(10^3)$. The flagella of sperm, with a diameter of 250 nm and a transverse velocity of 300 μm/s experience a $We = O(10^6)$ [Ishijima *et al.* (1986)]. We therefore surmise that these driven magnetic bead studies can yield insights into understanding hydrodynamic physiological phenomena, such as mucus clearance, infection, and fertility.

ACKNOWLEDGMENTS

The authors acknowledge research support from NHLBI(P41-EB002025), NIBIB(R01-HL077546), NSF DMS-0908423, DMR-1122483, DOE DE-SC0001914, and NSF DMS-1100281. They thank Gareth H. McKinley for helpful modeling suggestions.

References

Arigo, M. T., D. Rajagopalan, N. Shapley, and G. H. McKinley, "The sedimentation of a sphere through an elastic fluid. Part 1. Steady motion," J. Non-Newtonian Fluid Mech. **60**, 225–257 (1995).

Bird, R., C. Curtiss, R. Armstrong, and O. Hassager, *Dynamics of Polymeric Liquids: Fluid Mechanics* (Wiley, New York, 1987).

Buhler, E., and F. Boué, "Chain persistence length and structure in hyaluronan solutions: Ionic strength dependence for a model semirigid polyelectrolyte," Macromolecules **37**, 1600–1610 (2004).

Celli, J. P., B. S. Turner, N. H. Afdhal, S. Keates, I. Ghiran, C. P. Kelly, and R. Bansil, "Helicobacter pylori moves through mucus by reducing mucin viscoelasticity," Proc. Natl. Acad. Sci. U.S.A. **106**, 14321–14326 (2009).

Cribb, J. A., T. D. Meehan, S. M. Shah, K. Skinner, and R. Superfine, "Cylinders vs. spheres: Biofluid shear thinning in driven nanoparticle transport," Ann. Biomed. Eng. **38**, 3311–3322 (2010).

Fisher, J. K., J. A. Cribb, K. V. Desai, L. Vicci, B. Wilde, K. Keller, and R. Superfine, "Thin-foil magnetic force system for high-numerical-aperture microscopy," Rev. Sci. Instrum. **77**, 023702 (2006).

Fu, H. C., V. B. Shenoy, and T. R. Powers, "Role of slip between a probe particle and a gel in microrheology," Phys. Rev. E **78**(6), 061503 (2008).

Hill, D. B., V. Swaminathan, A. Estes, J. A. Cribb, E. T. O'Brien, C. W. Davis, and R. Superfine, "Force generation and dynamics of individual cilia under external loading," Biophys. J. **98**, 57–66 (2010).

Ishijima, S., S. Oshio, and H. Mohri, "Flagellar movement of human spermatozoa," Gamete Res. **13**, 185–197 (1986).

King, M., and P. T. Macklem, "Rheological properties of microliter quantities of normal mucus," J. Appl. Physiol. **42**, 797–802 (1977).

Likhtman, A. E., and R. S. Graham, "Simple constitutive equation for linear polymer melts derived from molecular theory: Rolie–Poly equation," J. Non-Newtonian Fluid Mech. **114**, 1–12 (2003).

Lu, Y., B. Weers, and N. C. Stellwagen, "DNA persistence length revisited," Biopolymers **61**, 261–275 (2002).

McKinley, G. H., "Steady and transient motion of spherical particles in viscoelastic liquids," in *Transport Processes in Bubble, Drops, and Particles*, edited by D. de Kee and R. P. Chhabra (Taylor & Francis, New York, 2002), pp. 338–375.

Meyer, A., A. Marshall, B. G. Bush, and E. M. Furst, "Laser tweezer microrheology of a colloidal suspension," J. Rheol. **50**, 77–92 (2006).

Morris, G. A., T. R. Patel, D. R. Picout, S. B. Ross-Murphy, A. Ortega, J. Garcia de la Torre, and S. E. Harding, "Global hydrodynamic analysis of the molecular flexibility of galactomannans," Carbohydr. Polym. **72**, 356–360 (2008).

Owens, R. G., and T. N. Phillips, *Computational Rheology* (Imperial College Press, London, 2002).

Pozrikidis, C., *Introduction to Theoretical and Computational Fluid Dynamics* (Oxford University Press, New York, 1997).

Puchelle, E., J. M. Zahm, and D. Quemada, "Rheological properties controlling mucociliary frequency and respiratory mucus transport," Biorheology **24**, 557–563 (1987).

Rajagopalan, D., M. T. Arigo, and G. H. McKinley, "The sedimentation of a sphere through an elastic fluid Part 2. Transient motion," J. Non-Newtonian Fluid Mech. **65**, 17–46 (1996).

Rich, J. P., J. Lammerding, G. H. McKinley, and P. S. Doyle, "Nonlinear microrheology of an aging, yield stress fluid using magnetic tweezers," Soft Matter **7**, 9933–9943 (2011).

Rubin, B. K., "The pharmacologic approach to airway clearance: Mucoactive agents," Paediatr. Respir. Rev. **7**, S215–S219 (2006).

Squires, T. M., "Nonlinear microrheology: Bulk stresses versus direct interactions," Langmuir **24**, 1147–1159 (2008).

Squires, T. M., and J. F. Brady, "A simple paradigm for active and nonlinear microrheology," Phys. Fluids **17**, 073101 (2005).

Squires, T. M., and T. G. Mason, "Fluid mechanics of microrheology," Annu. Rev. Fluid Mech. **42**, 413–438 (2010).

Sriram, I., E. M. Furst, R. J. DePuit, and T. M. Squires, "Small amplitude active oscillatory microrheology of a colloidal suspension," J. Rheol. **53**, 357–381 (2009).

Teixeira, R. E., A. K. Dambal, D. H. Richter, E. S. Shaqfeh, and S. Chu, "The individualistic dynamics of entangled DNA in solution," Macromolecules **40**, 2461–2476 (2007).

Uhde, J., W. Feneberg, N. Ter-Oganessian, E. Sackmann, and A. Boulbitch, "Osmotic force-controlled microrheometry of entangled actin networks," Phys. Rev. Lett. **94**, 198102 (2005).

Wilking, J. N., and T. G. Mason, "Optically driven nonlinear microrheology of gelatin," Phys. Rev. E **77**, 055101 (2008).

Ziemann, F., J. Rädler, and E. Sackmann, "Local measurements of viscoelastic moduli of entangled actin networks using an oscillating magnetic bead micro-rheometer," Biophys. J. **66**, 2210–2216 (1994).